

# RSC Advances



This is an *Accepted Manuscript*, which has been through the Royal Society of Chemistry peer review process and has been accepted for publication.

*Accepted Manuscripts* are published online shortly after acceptance, before technical editing, formatting and proof reading. Using this free service, authors can make their results available to the community, in citable form, before we publish the edited article. This *Accepted Manuscript* will be replaced by the edited, formatted and paginated article as soon as this is available.

You can find more information about *Accepted Manuscripts* in the [Information for Authors](#).

Please note that technical editing may introduce minor changes to the text and/or graphics, which may alter content. The journal's standard [Terms & Conditions](#) and the [Ethical guidelines](#) still apply. In no event shall the Royal Society of Chemistry be held responsible for any errors or omissions in this *Accepted Manuscript* or any consequences arising from the use of any information it contains.

## Experimental optimization of a passive planar rhombic micromixer with obstacles for effective mixing in a short channel length

Iwona Bernacka-Wojcik,<sup>\*a</sup> Susana Ribeiro,<sup>b</sup> Pawel Jerzy Wojcik,<sup>a</sup> Pedro Urbano Alves,<sup>a</sup> Tito Busani,<sup>a</sup> Elvira Fortunato,<sup>a</sup> Pedro Viana Baptista,<sup>c</sup> José António Covas,<sup>b</sup> Hugo Águas,<sup>\*a</sup> Loic Hilliou<sup>\*b</sup> and Rodrigo Martins<sup>a</sup>

<sup>a</sup>CENIMAT/I3N, Departamento de Ciência dos Materiais, Faculdade de Ciências e Tecnologia, Universidade Nova de Lisboa and CEMOP-UNINOVA, Campus de Caparica, 2829-516 Caparica, Portugal

<sup>b</sup>IPC/I3N, Dept. Polymer Engineering, Universidade do Minho, Campus de Azurém, 4800-058 Guimarães, Portugal

<sup>c</sup>CIGMH, Departamento de Ciências da Vida, Faculdade de Ciências e Tecnologia, Universidade Nova de Lisboa, Campus de Caparica, 2829-516 Caparica, Portugal

Corresponding authors:

I. Bernacka-Wojcik [ib@uninova.pt](mailto:ib@uninova.pt); L. Hilliou [loic@dep.uminho.pt](mailto:loic@dep.uminho.pt); H. Águas [hma@fct.unl.pt](mailto:hma@fct.unl.pt)

Tel.: +351 212948525

## Abstract

This paper presents the performance of a passive planar rhombic micromixer with diamond-shaped obstacles and a rectangular contraction between the rhombi. The device was experimentally optimized using water for high mixing efficiency and low pressure drop over a wide range of Reynolds numbers ( $Re = 0.1-117.6$ ) by varying geometrical parameters, such as number of rhombi, distance between obstacles and contraction width. Due to the large amount of data generated, statistical methods were used to facilitate and improve the results of the analysis. The results revealed a rank of factors influencing mixing efficiency: Reynolds number > number of rhombi > contraction width > inter-obstacles distance. The pressure drop measured after three rhombi depends mainly on  $Re$  and inter-obstacles distance. The resulting optimum geometry for low  $Re$  regime has a contraction width of 101  $\mu\text{m}$  and inter-obstacles distance of 93  $\mu\text{m}$ , while for high  $Re$  regime, a contraction width of 400  $\mu\text{m}$  and inter-obstacles distance of 121  $\mu\text{m}$ ) are more appropriate. These mixers enabled 80% mixing efficiency creating a pressure drop of 6.0 Pa at  $Re = 0.1$  and  $5.1 \times 10^4$  Pa at  $Re = 117.6$ , with a mixer length of 2.5 mm. To the authors' knowledge, the developed mixer is one of the shortest planar passive micromixers reported to date.

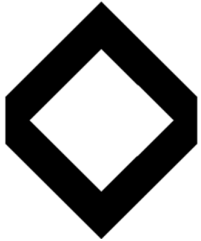
**Keywords:** microfluidics; micromixer; pressure drop; obstacles; rhombic microchannel; Response Surface Methodology

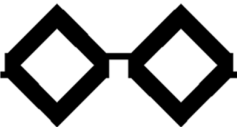
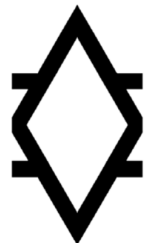
## 1. Introduction

Miniaturisation is a recent trend in analytical chemistry and life sciences due to the possibility of performing sophisticated analysis within a hand hold size, faster sample analysis, higher throughput, portability, reduced reagent use, all of which are associated with decreased cost. However, physical and chemical surface effects such as capillary forces, surface roughness and chemical interactions of construction materials with reaction processes, become more dominant at the micro-scale<sup>1</sup>, thus impeding a simple scaling down approach of existing mixing systems. For microfluidic systems, the Reynolds number ( $Re$ ) is typically smaller than 100 and the flow is considered essentially laminar, which critically limits mixing efficiency<sup>2</sup>. Convective mass transfer occurs only in the fluid flow direction and mixing is achieved merely by molecular diffusion. However, diffusion alone is inefficient and imposes the need of long microchannels, meaning that mixing at the micro-scale should be artificially enhanced. Accordingly, two basic principles are exploited to enhance mixing at the micro-scale: active or passive<sup>2</sup>. Active mixers depend on an external energy source to achieve mixing, whereas passive mixers solely rely on fluid pumping energy and use special channel designs to restructure the flow, reduce the diffusion length and maximize the contact surface area between fluids<sup>3</sup>.

In contrast to active micromixers or three-dimensional passive micromixers, planar passive micromixers are more cost efficient, can be easily integrated with other microfluidic components and can be fabricated using conventional single layer photolithography techniques. As such, research for achieving best mixing efficiency in the shortest time and smallest pressure drop using planar passive micromixers has thrived during the last decade. The field is often reviewed, see for instance<sup>2-5</sup>. Table 1 summarizes the main types of existing passive planar micromixers, with the corresponding best mixing efficiencies reported to date, relying essentially on chaotic advection to mix water-based fluids with Newtonian behaviour. This table is certainly not a comprehensive review of designs and performance, but its content can serve to appraise mixing efficiencies, pressure drops and mixing distances achieved with innovative micromixer designs. All microchannel designs summarized in Table 1 rely on the split and recombine concept and/or on chaotic advection where obstacles or baffles are inserted along the channel to promote converging and diverging flows. Interestingly, only four out of fourteen designs use curvilinear channels to enhance secondary flows in the curves. Such flows usually result from the elasticity of the fluid rather than from inertial effects; thus, they should be promising in enhancing mixing when viscoelastic fluids such as polymer solutions are used<sup>6</sup>.

Table 1. Summary of planar passive micromixer designs with respective performance reported in the literature(\* data obtained through simulations).

chip design <sup>ref.</sup>	mixing length (mm)	channel width ( $\mu\text{m}$ )	channel depth ( $\mu\text{m}$ )	<i>Re</i> range	best mixing performance (corresponding <i>Re</i> )	pressure drop in Pa (corresponding <i>Re</i> )	schematic
Y-rectangular mixer <sup>7</sup>	40.0	250	292	10–1000 (1 ml/min–18 ml/min)	~ 100% (not available; 8 ml/min)	~ $9.0 \times 10^4$ (not available; 8 ml/min)	
rectangular channel with triangle-shaped mixing elements <sup>8</sup>	32.0	150	50	0.1–20.0	90% (0.1 and 20)	not available	
rhombic (angle $90^\circ$ ) with a converging-diverging element <sup>9</sup>	13.3	250	130	5–200	80% (5) 94% (200)	$1.6 \times 10^2$ (10)* $5.7 \times 10^3$ (200)*	
rectangular channel with diamond-shaped obstacles <sup>10</sup>	11.0	200	55	0.02–10.00	90% (0.1)	$1.5 \times 10^2$ (0.1)*	
curved channels with unbalanced splits and collisions of streams <sup>11</sup>	8.0	300 (sum of sub-channels width)	120	10–80	64% (80)	not available	
rectangular channel with baffles <sup>12</sup>	8.0	400 (50–150 for baffle)	130	40–80	> 90% (80)	$3.1 \times 10^4$ (80)*	
labyrinth: “S-shaped” mixers with $180^\circ$ turns <sup>13</sup>	7.3	220	267	2.5–30.0	80% (5)	not available	
rhombic (angle $60^\circ$ ) with a converging-diverging element <sup>14</sup>	6.8	250 (100 for converging-diverging element)	130	0.1–110.0	86% (0.1) 85% (110)	$1.2 \times 10^1$ (0.1)* $2.1 \times 10^4$ (110)*	

rhombic (angle 90°) with asymmetrical constriction between rhombi <sup>15</sup>	4.8	250 (88–700 for constrictions)	120	1–50	90% (20)	$3.6 \times 10^3$ (20)*	
C-shape channel with baffles <sup>16</sup>	3.6	130 (40 for baffles)	130	1–100	85% (81)	$3.4 \times 10^4$ (81)*	
rectangular channel with baffles and gaps <sup>17</sup>	2.4	400 (50–150 for gaps)	120	0.1–30.0	91% (0.1) 94% (30)	$1.5 \times 10^1$ (0.1)* $1.5 \times 10^2$ (1)* $1.3 \times 10^4$ (40)*	
modified square wave mixer with by-passes <sup>18</sup>	1.9 per repeating unit	200–400	200	not available (0.1 ml/min–14 ml/min)	87% (not available; 0.2 ml/min)	$7.0 \times 10^3$ per repeating unit (not available; 4.0 ml/min)	
rhombic (angle 60°) with branch channels <sup>19</sup>	not available	250 (100 for branch channels)	120	10–120	98% (120)	$9.0 \times 10^3$ (120)*	
rhombic (angle 60°) with diamond-shaped obstacles and rectangular contractions (this paper)	2.5	200	130	0.1–117.6	80% (0.1 and 117.6)	6.0 (0.1) $5.1 \times 10^4$ (117.6)	

Ubiquitous to all studies reported in Table 1 is the occurrence of a minimum in mixing efficiency for Reynolds numbers in the range of 1 to 10. This is related to the transition from diffusion to advection driven mixing. Also, all these mixers were optimized using computational fluid dynamics simulations, only the best designs having been fabricated and experimentally tested for mixing efficiency. Only Kashid *et al.*<sup>7</sup> and Goovaerts *et al.*<sup>18</sup> have measured experimentally the pressure drop, while the others reported data obtained exclusively from simulations. Although simulations can provide valuable qualitative and quantitative predictions significantly reducing time and cost, it is difficult to access their uncertainty, as the results are affected by the accuracy of modelling, discretization and iteration. For instance, Matsunaga *et al.*<sup>20</sup> have shown that for a T-shaped micromixer operating in the *Re* range

of 140–250, grid-based simulations may overestimate mixing efficiency by up to 30%. Therefore, this paper is based exclusively on the experimental characterisation of micromixers. We present a passive planar rhombic micromixer<sup>9</sup> with obstructions in the microchannel<sup>10</sup> and a contraction placed after each rhombus to further increase interface generation between fluid elements. All these mixing elements (i.e. rhombic channel; obstructions and contractions) enhance mixing through stretching, folding, and break-up processes caused by transverse flows. Rhombic channels induce recirculation at each angle and should also promote curved fluid streams in the rhombus tips. Such curved streams should enhance elastic instabilities and turbulences, and will be further used in a future study focusing on the mixing efficiency and pressure drop optimization for viscoelastic fluids. In addition, a rectangular contraction (called elsewhere “gap”<sup>10</sup>) is placed after each rhombus to enhance extensional flows which are known for significantly improving the mixing in viscoelastic fluids<sup>21</sup>. The aim of this study is to experimentally optimize the micromixer design by varying geometrical parameters and to identify the most relevant ones for obtaining the best mixing efficiency and shortest mixing length with minimal pressure drop for Newtonian fluids. We investigate the influence of the diamonds distance ( $d$ ) and contraction width ( $w_c$ ) on mixing efficiency and pressure drop over a wide range of flow conditions. For each chip, the total pressure drop and mixing efficiencies at three locations along the channel were measured for twelve  $Re$  values ranging from 0.1 to 117.6. Due to the complexity of the study and the number of studied responses, statistical methods were used to facilitate and improve the data analysis.

## 2. Experimental details

### 2.1. Fabrication of microfluidic device

The mould for PDMS patterning was fabricated by ultraviolet photolithography in SU-8 2050 (Microchem, USA). The material was spin-coated on silicon wafers at 1530 rpm to form a  $\sim 130$   $\mu\text{m}$  thick layer, then soft baked on a levelled hot plate for 5 min at 65 °C and then for 24 min at 95 °C. After cooling (10 min), the samples were UV exposed on a mask aligner (MA6, Suss MicroTec, Germany) for 21 s with an exposure dose of  $\sim 309$   $\text{mJ}/\text{cm}^2$  through an i-line filter (G180336, Suss MicroTec, Germany). Then, the samples were post-baked during 5 min at 65 °C and subsequently for 11 min at 95 °C. Patterns were developed by submersing them in PGMEA (Microchem, USA) during 18 min with magnetic agitation of 500 rpm, rinsing them with IPA and gently drying with compressed nitrogen. The mould was silanized with tridecafluoro-1,1,2,2-tetrahydrooctyl trichlorosilane (Microchem, USA).

PDMS (Sylgard 184, Dow Corning, Spain) was prepared by mixing a base and a curing agent in a 10:1 weight ratio. The mixture was stirred and de-gassed in a vacuum desiccator. Afterwards, the

PDMS was poured over the SU-8 mould and cured at 100 °C on a levelled hot plate for 3 hours. Then, the PDMS was peeled off from the SU-8 mould.

The PDMS structures were placed on top of a Petri dish with the negative relief features up. On top of the features of the PDMS structure, an epoxy glue (ES562, Permabond) was poured to form a ~2 mm thick layer. After ~72 h degassing in a desiccator, the epoxy glue was cured in an oven at 120 °C for ~40 min. Then, the cured epoxy was peeled from the PDMS and utilized as a master mould for PDMS soft lithography using the same procedure as described above. The inlets and outlets of the PDMS chips were made using a blunt needle. The chips were irreversibly bonded to glass slides by plasma oxygen (60 s in 13 Pa, 100 W, Plasma electronic Buck Technologiien, Germany). After the plasma treatment, the PDMS-glass sandwich was baked at 100 °C for 5 min to increase the bond strength.

The chips were characterized by optical microscopy (Leitz Laborlux 12 ME ST), profilometry (XP-200, Ambios Technology, Inc., Santa Cruz, USA) and scanning electron microscopy (SEM, Zeiss Auriga, Germany).

## 2.2. Assessment of mixing efficiency

Two fluids were supplied to the microchannels using a syringe pump (Harvard Apparatus PHD 22/200) with two syringes (Hamilton 1005LNTN, USA) with 5.0 ml and 2.5 ml capacity. During the experiments, the first syringe was filled with a blue dye (food grade dye, E133) at a 20 times dilution in deionized water and the 2.5 ml syringe was filled with deionized water only. The two syringes were driven at flow rates ranging from 0.06 ml/h ( $Re = 0.1$ ) to 56.00 ml/h ( $Re = 117.6$ ), measured in separated calibration runs where volumetric flow rates were recorded using gravimetric balances at the micromixers' outlet. The image capturing system consists of an inverted microscope (Leica DMI 5000M, Leica Microsystems, Germany) connected to a light sensitive CCD camera (Lu160, Lumenera Corporation, USA). Images were processed using ImageJ software to quantify the mixing index and mixing efficiency. The concentration  $c_i$  at an image point is represented by the pixel intensity value  $I_i$ , with the limiting values of concentration  $c_{\max}$  and  $c_{\min}$  corresponding to  $I_{\max}$  and  $I_{\min}$ , respectively. Pixel intensity values were normalized according to eq. 1.

$$\bar{I}_i = \frac{I_i - I_{\min}}{I_{\max} - I_{\min}} \quad \text{eq. (1)}$$

The mixing index ( $\sigma$ ) is defined as the standard deviation of the pixel intensity distribution along a line (see Fig. 1C) across the micromixer channel<sup>22</sup>:

$$\sigma = \sqrt{\langle (\bar{I}_i - \langle \bar{I} \rangle)^2 \rangle} \quad \text{eq. (2)}$$

where  $\bar{I}_i$  is the normalized grey-scale pixel intensity given by eq. 1 (between 0 and 1) and  $\langle \bar{I} \rangle$  is the normalized average greyscale intensity. The value of  $\sigma$  is 0.5 for completely segregated (unmixed)

streams at micromixer entrance and 0 for perfectly mixed streams. The mixing efficiencies ( $M$ ) were then calculated from  $\sigma$  using<sup>17</sup>:

$$M = 100 \times \left(1 - \frac{\sigma}{\bar{I}}\right) \quad \text{eq. (3)}$$

where  $\langle \bar{I} \rangle \approx 0.40 \pm 0.05$ , due to asymmetric inlets' configuration. The uncertainty of  $M$  determination comes mainly from accuracy of image analysis (pixels noise), reproducibility of image analysis (2 snapshots were taken at 2 different instants, thus averaging possible fluid fluctuations) and chip construction reproducibility (some measurements were repeated in a second chip with the same configuration). The combined  $M$  determination uncertainty is 6.6% originating largely from pixels noise.

The  $Re$  number was calculated with the following expression:

$$Re = \frac{2\rho Q}{(W_c+h)\eta_0} \quad \text{eq. (4)}$$

in which  $\rho$  is the density of water (998 kg/m<sup>3</sup>),  $Q$  is the volumetric flow (m<sup>3</sup>/s),  $w_c$  is the width ( $2 \times 10^{-4}$  m) of the equivalent rectangular channel and  $h$  is the height ( $1.3 \times 10^{-4}$  m), and  $\eta_0$  is the viscosity of the dyed water ( $8 \times 10^{-4}$  Pa  $\times$  s) measured at 28 °C (the temperature at which both mixing efficiency and pressure drop were measured) using a stress controlled rotational rheometer (MCR300, Paar Physica) equipped with concentric cylinders (CC27, Paar Physica). Within the detection limit of the rheometer and the shearing geometry used, we noted no difference between the viscosity of the dyed fluid and the viscosity of the deionized water.

## 2.2. Pressure drop measurements

Pressure drop was measured using a differential pressure transducer (26PC, Honeywell, USA) connected to the pressure taps of the micromixer with flexible Tygon tube (internal diameter 0.8 mm). The transducer voltage output was digitized (NI 9215, National Instruments, USA) and further processed using a home-written LabView routine enabling the on-the-fly oversampling of data, resulting in an increased sensitivity of the transducer<sup>23</sup>. The transducer (with tubing) was calibrated using a pressure pump (MFCS-100, Fluigent, France) in the range  $7 \times 10^2$ – $1 \times 10^5$  Pa.

## 2.3. Statistical analysis

Statistical data analysis was performed using JMP 8.01 software (S.A.S. Institute Inc., Cary, NC, USA). Graphical presentations of the models were generated in JMP 8.01 and processed graphically in OriginPRO 8.5 2010 (OriginLab Corporation, Northampton, MA, USA) diagramming tool. The information to support the developed work can be found in Supplementary information.

### 3. Results and discussion

#### 3.1. Mixer design and fabrication

The proposed mixer enhances mixing by three means: (i) obstacles within the microchannel; (ii) rhombic channel structure and (iii) contraction in between rhombi (Fig. 1A). The inlet channel of fluid A is split into 2 channels with a width of 200  $\mu\text{m}$ , while the inlet and outlet channels of fluid B are 2000  $\mu\text{m}$  long and 400  $\mu\text{m}$  wide. The diameter of inlets and outlet is 1000  $\mu\text{m}$ . Additionally, 2 mm away from the inlet B and outlet, pressure taps (diameter: 1000  $\mu\text{m}$ ) were placed for measurement of pressure drop.

The presence of obstacles alters the flow direction, inducing recirculation that causes transversal mass transport. Large recirculation is beneficial for increased interfacial contact area between two species improving diffusion-based and convective mixing. Proper configuration of obstacles is critical, e.g. symmetric obstacles reduce the contact surface leading to lower mixing efficiency than in the absence of obstacles<sup>24</sup>. Generally, obstacles are efficient mainly for fast flows (usually at  $Re$  above 10) and only optimized geometries (i.e. diamond-shaped<sup>10</sup> or asymmetric rectangles<sup>25</sup>) enable satisfactory mixing at  $Re$  below 1. Diamond-shaped obstacles provide better mixing performance than circular- or triangular-shaped obstructions because they split the flow without introducing stagnation areas inside the channel. Furthermore, stepping of the walls of the diamond-shaped obstructions improves mixing efficiencies<sup>10</sup>. Therefore, diamond-shaped obstacles (100  $\mu\text{m} \times 100 \mu\text{m}$ ; width  $\times$  length) with 20  $\mu\text{m}$  steps were positioned inside a microchannel (200  $\mu\text{m} \times 125 \mu\text{m}$ ; width  $\times$  height) with an offset of 30  $\mu\text{m}$ . Since the obstacles occupy the whole depth of the channel, the chip mould can be processed in a single photolithography step. This is of extreme relevance when prototyping and scale up production are concerned.

At very low  $Re$  (below 1), micromixers based on diamond-stepped obstacles require a long mixing channel (about 11 mm). A rhombic channel structure was therefore adapted to induce recirculation at rhombus corners<sup>14</sup>. When  $Re$  is high enough, vortices may be created at the rhombus turns, increasing the advective transport. The average velocity in the rhombic mixer is only half of that on the zigzag mixer, yielding a lower pressure drop. A turning angle of the rhombic mixer of 60° was chosen, as it is the best compromise between mixer footprint, induced dead volume and mixing efficiency<sup>14</sup>. The length of the rhombic period is fixed at 1500  $\mu\text{m}$ , while the length of the contraction between rhombi is 100  $\mu\text{m}$ .

Once the fluid flows out of the rhombic channel, two streams merge into a single one by means of a contraction and accelerate due to smaller cross-sectional area. After passing the contraction, flow is decelerated and separated into two streams. The added contraction can provide better mixing

efficiency at lower  $Re$  by increase of the interfacial area due to stretching and at higher  $Re$  by recirculation and vortices<sup>14</sup>. Here, a rectangular contraction was used as this configuration resulted in the shortest mixer length and one of the highest mixing efficiencies reported so far for planar passive mixers<sup>17</sup> (see Table 1).

To optimize the mixer performance (in terms of lower pressure drop and shorter length), various mixer configurations were tested, where the controlled variables are the number of rhombi (1, 2 and 3), the width of the contraction between rhombi ( $w_t = 100\text{--}400\ \mu\text{m}$ ) and the distance between stepped diamond-shaped obstacles ( $d = 60\text{--}140\ \mu\text{m}$ ). There were 9 chips configurations of various combinations of  $w_t$  and  $d$ . The mixing efficiency was analysed after each rhombus to evaluate the influence of the number of rhombi.

The micromixers were fabricated in PDMS by a replica moulding technique using a mould produced in SU-8 by UV photolithography<sup>26</sup>. SU-8 moulds suffer delamination at the photoresist-substrate interface after fabrication of few PDMS replicas, therefore we have used an intermediate monolithic epoxy mould to increase the number of possible PDMS replicas from the same SU-8 mould. The moulding process starts with the fabrication of an SU-8 mould, then instead of casting PDMS repeatedly from this mould, PDMS is casted once and used as mould for patterning of an epoxy mould, which can then be used to produce many PDMS replicas without suffering from the delamination problem. The SEM image (Fig. 1B) confirms the good definition of the PDMS features. The PDMS replicas obtained by this process are about 5% smaller than the designed dimensions due to PDMS shrinkage<sup>27</sup>, i.e. the obstacles width is  $95\ \mu\text{m}$  instead of the intended  $100\ \mu\text{m}$ . Fig. 1B presents also a photograph of the microfluidic mixer filled with dyes for better visualization.

(position for Fig. 1)

Fig. 1(A) Schematic diagram of the designed rhombic micromixer with stepped diamond-shaped obstacles and rectangular contractions between rhombi. (B) PDMS micromixer fabricated using SU-8 mould and epoxy mediating mould. (C) Optical microscopy images taken at different locations along a micromixer with  $w_t = 100\ \mu\text{m}$  and  $d = 140\ \mu\text{m}$  at  $Re = 8.2$ . Mixing efficiency was analysed along the channel in the middle of the first contraction,  $M(1)$ , second contraction,  $M(2)$  and third contraction,  $M(3)$ , as indicated by the vertical dotted lines.

### 3.2. Mixing efficiency and mechanism

Fig. 1C displays representative snapshots captured for a micromixer ( $w_t = 250\ \mu\text{m}$  and  $d = 140\ \mu\text{m}$ ) operated at  $Re = 8.2$ . At the entrance of the first rhomb, the light grey corresponds to pure water,

while the darker grey corresponds to the dyed water. As the two fluids flow along the channel, increased mixing is apparent. For each chip, the mixing efficiency in the middle of the first contraction,  $M(1)$ , second contraction,  $M(2)$  and third contraction,  $M(3)$  were measured for various  $Re$ . Furthermore,  $M$  at the outlet channel was measured, but no increase was observed, probably due to a short distance (100  $\mu\text{m}$ ) from the  $M(3)$  access line. To assess the mixing mechanism, images of the micromixers with  $w_t$  from 100 to 400  $\mu\text{m}$  were compared at various  $Re$ .  $Re$  of 1.2; 5.9 and 88.2 were chosen to better visualize the fluid behaviour. At  $Re = 0.1$  and  $Re = 117.6$ , the fluids at the first contraction are already significantly mixed by means of the obstacles, so the grey-scale contrast between fluids is much lower. Fig. 2A presents optical microscopy images taken at the first contraction of a micromixer of  $d = 140 \mu\text{m}$ , revealing the effect of  $w_t$  on the flow for various  $Re$ . Passing through the contraction, the flow is accelerated and decelerated afterwards. At  $Re = 1.2$  and  $Re = 5.9$ , the flow is laminar and mixing is enhanced only by the increased contact between fluids. At the lowest  $Re$  (1.2), mixing is better than in the case of  $Re = 5.9$  due to increased residence time. At higher  $Re$  (88.2), there is stronger fluid agitation and the flow is greatly affected by the contraction width. At the lowest contraction width ( $w_t = 100 \mu\text{m}$ ), after flowing through the contraction, the water stream is transferred from the inner channel walls towards the outer walls, improving mixing. The flow features were observed for the rectangular contraction by Bhagat *et al.*<sup>10</sup> and can be explained by the formation of vortices. The size of the contraction is critical for the vortices formation at the exit of the contraction: in mixers of  $d = 140 \mu\text{m}$ , for  $w_t = 100 \mu\text{m}$ , vortices are generated starting from  $Re = 29.4$ ; for  $w_t = 250 \mu\text{m}$ , vortices are formed only at  $Re = 117.6$ , while for  $w_t = 400 \mu\text{m}$ , vortices are not observed in any of the tested flow conditions. Fig. 2B shows a comparison of the vortices generated at  $Re = 28.4$ ;  $Re = 58.8$  and  $Re = 117.6$  in the mixer with  $w_t = 100 \mu\text{m}$  and  $d = 140 \mu\text{m}$ . The size and intensity of the generated vortices increase significantly with  $Re$  enhancing mixing.

(position for Fig. 2)

Fig. 2. Optical microscopy images taken at the first contraction for various flow conditions. (A) Influence of the contraction width ( $w_t$ ) on fluid mixing at  $Re = 1.2$ ;  $Re = 5.9$  and  $Re = 88.2$ , in mixers with inter-obstacles distance  $d = 140 \mu\text{m}$ . At lower  $w_t$  and higher  $Re$ , strong acceleration and subsequent deceleration of flows leads to formation of vortices. (B) Comparison of vortices generated at  $Re = 28.4$ ;  $Re = 58.8$  and  $Re = 117.6$  in mixer with  $w_t = 100 \mu\text{m}$ . (C) Influence of the inter-obstacles distance ( $d$  varying from 60  $\mu\text{m}$  to 140  $\mu\text{m}$ ) for micromixers with  $w_t = 400 \mu\text{m}$  at  $Re = 5.9$ . For  $d = 60 \mu\text{m}$ , the fluids flow mainly next to the channel walls due to low inter-obstacles channel width.

The effect of  $d$  on mixing at  $Re = 5.9$  in mixers with  $w_t = 400 \mu\text{m}$  is visualized in Fig. 2C. The images indicate that for the mixer with  $d = 60 \mu\text{m}$ , water flows mainly next to the channel walls due to small

inter-obstacles channel width (i.e. 20  $\mu\text{m}$ ; equal to the distance obstacle-channel wall). For  $d$  above 100  $\mu\text{m}$ , the inter-obstacles channel width is much larger enabling water to flow in between the obstacles, splitting and recombining the streams with dyed water.

Fig. 3 presents the mixing efficiency ( $M$ ) of chips of various configurations. In all cases, the dependence between  $M$  and  $Re$  shows a minimum at  $Re = 5.9$ . Below this value, the lower the  $Re$  the longer the residence time and the better the mixing by pure diffusion<sup>10</sup> (see Fig. 2A for comparison of mixing state at  $Re = 1.2$  and  $Re = 5.9$ ). Above  $Re = 5.9$ , the mixing efficiency increases with  $Re$  due to the stronger fluid agitation and higher advection. The chip with  $w_t = 400 \mu\text{m}$  and  $d = 100 \mu\text{m}$  shows non-consistent mixing efficiency results, possibly due to fabrication or mixing measurement issues, thus this chip was not taken into account in the analysis.

(position for Fig. 3)

Fig. 3. Experimental mixing efficiency ( $M$ ; given in %) of mixers with various configurations at the middle of the first contraction ( $M(1)$ ; red line), second contraction ( $M(2)$ ; blue line) and third contraction ( $M(3)$ ; green line). Data points labelled  $a$  and  $b$  were determined from two different images taken from the first chip, while data points labelled  $c$  and  $d$  were determined from two different images taken from the second chip. Connecting lines are for eye guidance only.

In order to better understand the mixing mechanism and the role of  $d$ ,  $w_t$  and number of rhombi, an efficient mathematical methodology based on statistical techniques was applied for the analysis of the large amount of data displayed in Fig. 3 (see section 3.4).

### 3.3. Pressure drop

Firstly, the experimental protocol of the pressure drop ( $dP$ ) measurements was validated by estimating the viscosity of water computed from the pressure drop measured at 28  $^{\circ}\text{C}$  for different flow rates, using the mixer that should develop larger pressures ( $w_t = 100 \mu\text{m}$ ;  $d = 60 \mu\text{m}$ ). This is needed to better match the pressure range that can be measured with the differential pressure transducer. The complex geometry of the developed mixer was simplified into a rectangular channel with length  $l$ , height  $h$  and width  $w$ . The wall shear stress ( $\tau$ ) was computed from  $dP$  using the following equation:

$$\tau = \frac{hdP}{2l\left(1+\frac{h}{w}\right)} \quad \text{eq. (5)}$$

where,  $l$  is the distance between the two pressure taps ( $l = 6800 \mu\text{m}$ ) and  $h$  is 120  $\mu\text{m}$  (as determined by stylus profilometry and optical microscopy).

The apparent shear rate ( $\dot{\gamma}_{app}$ ) was computed from the measured volumetric flow  $Q$  using the following equation (Newtonian flow):

$$\dot{\gamma}_{app} = \frac{6Q}{wh^2} \quad \text{eq. (6)}$$

The inset in Fig. 4A shows the log-log plot of the apparent shear rate as a function of the stress. A power law fitting to the data gives an exponent  $1.08 \pm 0.07$ , which indicates a Newtonian behavior<sup>28</sup>, confirming that no additional stress build up occurs in the micromixer in spite of the presence of converging and diverging flows. Similar conclusions were reached from  $dP$  measurements of water passing in a micron-sized contraction<sup>29</sup>. Thus, the approximation of the complex microchannel to a rectangular channel as proposed by equation 5 does not bring any error to the  $dP$  for the range of flow rates studied here. Accordingly, the stress computed in eq. (5) is error free as long as a correct effective channel width  $w$  is used (see below). The true shear rate ( $\dot{\gamma}$ ) is obtained by correcting the apparent shear rate using the following equation:

$$\dot{\gamma} = \frac{\dot{\gamma}_{app}}{3} \left( 2 + \frac{d \ln \dot{\gamma}_{app}}{d \ln \tau} \right) \quad \text{eq. (7)}$$

The viscosity ( $\eta$ ) is then obtained from the Newton relationship:

$$\tau = \eta \dot{\gamma} \quad \text{eq. (8)}$$

Essentially, viscosity data shown in Fig. 4A for the larger shear rates matches the viscosity values measured in separate measurements at 28 °C with a stress-controlled rotational rheometer. At lower shear rates, the shear viscosity shows some scattering due to the limit of sensitivity of the differential pressure transducer. We note that viscosity matching is achieved when an effective channel width of  $w = 32 \mu\text{m}$  is used in eq. 5 and 6. Thus, data in Fig. 4A indicate that the micromixer of dimensions  $w_t = 100 \mu\text{m}$ ;  $d = 60 \mu\text{m}$  can be used as a large shear rate rheometer for low viscosity liquids, since shear rates as large as  $2 \times 10^5 \text{ s}^{-1}$  can be achieved with no inertia instabilities, in contrast to conventional rotational rheometers.

Fig. 4B presents experimental  $dP$  results measured after three rhombi for all tested mixer configurations. Generally,  $dP$  increases linearly with  $Re$ , however for low  $Re$  (usually below 12), the pressure drop values were very close to the detection limit of the pressure sensor. Below  $2.0 \times 10^3 \text{ Pa}$ ,  $dP$  values are affected by the limit in pressure sensor sensitivity. Thus, a linear regression (intercept 0) of the  $dP$  data points measured at larger  $Re$  was used to extrapolate the  $dP$  for lower  $Re$ .

(position for Fig. 4)

Fig. 4(A) Shear rate dependence of the shear viscosity computed from the pressure drop ( $dP$ ) and the volumetric flow rate ( $Q$ ) measured with chip of  $w_t = 100 \mu\text{m}$ ;  $d = 60 \mu\text{m}$  for two values of the effective channel width ( $w$ ):  $20 \mu\text{m}$  (squares) and  $32 \mu\text{m}$  (triangles). The red dashed horizontal line

indicates the viscosity ( $8 \times 10^{-3} \text{ Pa} \times \text{s}$ ) of water at  $28 \text{ }^\circ\text{C}$  measured with a rotational rheometer. Inset: stress dependence of the apparent shear rate. The red line is a linear fit to the data with slope of  $1.08 \pm 0.07$  indicating a Newtonian behavior. (B) Experimental pressure drop ( $dP$ ) for micromixers of various configurations ( $w_t$  and  $d$  are given in  $\mu\text{m}$ ). (C) Zoom in on the low  $Re$  region. For low  $dP$  values (usually below 12), there is no linear dependence between  $dP$  and  $Re$  due to the detection limit of the pressure sensor.

### 3.4. Statistical analysis of the results

As it can be seen in Fig. 3 and Fig. 4, a large amount of data has been generated in this study, therefore to evaluate influence of the geometric parameters on the device performance for various flow regimes, statistical data treatment was used for the analysis of the results. The  $Re$  space was divided in two regions that can be approximated reasonably well by two independent Response Surface Methodology (RSM) models: low  $Re$  regime (from 0.1 to 5.9) and high  $Re$  regime (from 5.9 to 117.6). The analysis was focused on  $Re = 0.1$ , which is representative of typical micro-flow conditions<sup>10</sup> and also  $Re = 117.6$  for higher throughput applications. The model is fitted using RSM in order to:

- screen for the most important factors influencing the mixing efficiencies and pressure drop.
- build a mathematical model for all responses under consideration.
- develop a procedure to identify the most desirable conditions for mixer performance.

When considering all known mathematical models in which the response surface is continuous over the region being studied, the most suitable in this case seems to be a second-order (quadratic) ( $M(1)$ ;  $M(2)$ ;  $M(3)$  and  $dP$ ) model described in more details in Supplementary Information.

Model improvement for each response was evaluated based on a summary of fit (*i.e.* the least square regression) parameters summarized in Table S1 in Supplementary information. The experimental data points were sieved to eliminate those that do not follow the most pronounced trend, probably due to a gross error (for details, see Table S1 in Supplementary information). About 5% of all  $M$  data points were eliminated in sieving, increasing the  $R^2$  and  $R^2$ -adj parameters in an average of 0.02. In the case of the  $dP$  analysis, the  $R^2$  and  $R^2$ -adj were very high (0.98), therefore no data points were eliminated.

The second-order polynomial responses modelling (quadratic) offered by the RSM appeared to be sufficient for all responses under consideration due to the ability to supply a high coefficient of determination, *i.e.*  $R^2 = (0.96, 0.96, 0.96, 0.98)$  and  $R^2 = (0.91, 0.91, 0.91, 0.98)$  for  $M(1)$ ,  $M(2)$ ,  $M(3)$  and  $dP$  in low  $Re$  and high  $Re$  regime, respectively. Such high values of  $R^2$ , especially in a low  $Re$  regime, indicate good correspondence between the model prediction (fitting) and the experiments, while simultaneously minimizing the overall number of coefficients. The model for each response

was validated basing on analysis of  $F$ -ratio statistics ( $F$ -ratio) and the ANOVA probability ( $\text{Prob} > F$ ), indicating accuracy of the models for all responses (see details in Supplementary information).

Fig. 5 presents the results of mathematical fitting to the experimental data points of mixing efficiency (Fig. 5A–C) and pressure drop (Fig. 5D) for  $Re = 0.1$  and  $Re = 117.6$ . The mixing efficiency of 80% can be considered as full mixing<sup>30, 31</sup>.

(position for Fig. 5)

Fig. 5. Results obtained from mathematical fitting to the experimental data points (A) of mixing efficiency (given in %) measured at the middle of the first contraction ( $M(1)$ ); (B) at the second contraction ( $M(2)$ ); (C) at the third contraction ( $M(3)$ ) and (D) of pressure drop ( $dP$ ; given in kPa) measured after three rhombi. (E) Desirability results ( $D_n$ ) defined as maximum values of  $M(1)$ ;  $M(2)$  and  $M(3)$  and minimum of  $dP$ .

The results indicate that the number of rhombi has the strongest effect on the mixing index: generally,  $M$  increases with the number of rhombi, even if after the second rhombus the increase is much lower. After the first rhombus (mixer length: 0.9 mm), the mixing efficiency is below 80%, indicating that the fluids are not sufficiently mixed and that additional rhombi are needed (in fact, in the first rhombus the fluids are in contact only in a half of the rhomb, as the other half acts as inlet channel; see (Fig. 1A)). After the second rhombus (mixer length: 2.5 mm), the mixing efficiency is above 80% for all tested configurations. The third rhombus (mixer length: 4.1 mm) would further improve mixing (up to 85% for  $Re = 117.6$ ), however at the cost of a much longer channel (1.6 mm longer; i.e. 64% longer in the case of two rhombi mixer). Therefore a two rhombi mixer seems to give the best compromise between mixing efficiency and channel length.

At the first contraction, the mixing efficiency varies between 62.5% and 77.5% for the two analysed  $Re$ . At  $Re = 0.1$ ,  $M(1)$  is affected mainly by  $w_t$ : generally, smaller  $w_t$  gives better mixing, probably due to increased local Reynolds numbers and better contraction-expansion of stream lines.  $d$  is less significant for  $M(1)$  at  $Re = 0.1$ , as the obstacles have usually major effect on mixing for fast flows.  $d$  starts playing a more significant role for  $w_t$  above 250  $\mu\text{m}$ , where higher  $d$  values yield higher  $M(1)$ . In fact, the images shown in Fig. 2 indicate that in case of  $d = 60 \mu\text{m}$ , the hydraulic resistance between obstacles is too high, so the flow develops mainly close to the channel walls. Summarizing, at  $Re = 0.1$  the highest  $M(1)$  values are obtained for low  $w_t$  and low  $d$ , while the lowest  $M(1)$  occurs for high  $w_t$  and low  $d$ . At  $Re = 117.6$ , the lowest  $M(1)$  is also obtained for regions of high  $w_t$  and low  $d$ , whereas the highest  $M(1)$  is observed for high  $w_t$  and  $d$ .

For the same two  $Re$  values,  $M(2)$  and  $M(3)$  vary from 77.5 to 82.5%, therefore this variation range is very close to the range of uncertainty of the  $M$  determination ( $\pm 6.6\%$ ). Most probably, at the second and third contractions, all tested mixer configurations have yielded good mixing and the mixing efficiency saturates. In order to evaluate the effect of geometrical factors on  $M(2)$  and  $M(3)$ , a mixing analysis method of lower uncertainty of the  $M$  determination should be used, e.g. based on a fluorescent dye.

In Fig. 5A–C, the effect of the generation of vortices on the mixing state is not visible, as  $M(1)$  is measured in the middle of the first contraction (before the vortices are generated; see Fig. 2), whereas for  $M(2)$  and  $M(3)$  the range of mixing efficiency variation is very close to the  $M$  uncertainty range. Thus, to measure the effect of the vortices on the mixing state, the mixing efficiency should be measured in more locations along the chip.

The  $dP$  results obtained from the mathematical fitting (Fig. 5D) reveal that for  $Re = 0.1$  and  $Re = 117.6$ ,  $dP$  is mainly influenced by the inter-obstacles distance and the effect of  $w_i$  is barely visible. At  $Re = 0.1$ ,  $dP$  values are comparable with the values reported in literature (see Table 1): it varies from 10 to 138 Pa. The smallest  $dP$  are obtained for  $d$  between 77 and 125  $\mu\text{m}$ ; then, the  $dP$  values gradually increase for  $d$  values below and above this range. At  $Re = 117.6$ ,  $dP$  is much higher than at  $Re = 0.1$ : between  $4.6 \times 10^4$  Pa and  $8.6 \times 10^4$  Pa. As expected, the closer the obstacles, the higher  $dP$ . It should be noted that  $dP$  was measured for mixers with three rhombi (length: 4.1 mm), while our results indicate that two rhombi mixers (length: 2.5 mm) are sufficient to obtain satisfactory mixing for Newtonian fluids.

The tests of significance of all effects (i.e. factors and interactions) on mixing efficiencies and pressure drop were quantitatively performed using Student's  $t$ -test statistics. In general, the model predicts that mixing depends on  $Re$ , irrespectively of its value. However, only for  $M(1)$  this dependence seems to have a linear character. When considering geometrical factors,  $w_i$  affects mixing the most, while  $d$  seems to have a lower but still meaningful effect on the measured responses. Among all factors,  $Re$  was found to influence  $dP$  the most. This dependence seems to have a linear character. When considering geometrical factors,  $d$  nonlinearly affects  $dP$  significantly, while the role of  $w_i$  is negligible. The pattern of significance of all factors under consideration is similar for both  $Re$  regimes (i.e. significance pattern at low  $Re$  is a subset of the significance pattern at high  $Re$ ).

Response surface maps of experimental regions presented in Fig. 5 facilitate the decision-making process of determining the most appropriate geometry. However, a numerical multi-response optimization enables to find the specific point that maximizes the global desirability, and thus, the optimal performance of the mixer<sup>32</sup>. The desirability (i.e. optimization goal,  $D_n$ ) was defined as maximum values of  $M(1)$ ;  $M(2)$  and  $M(3)$  and minimum of  $dP$ . The contour plots of  $D_n$  at low and high  $Re$  regimes are presented in Fig. 5. The resulting optimum geometry determined from

desirability profiles is described by:  $w_t = 101 \mu\text{m}$ ,  $d = 93 \mu\text{m}$  at low  $Re$  regime and  $w_t = 400 \mu\text{m}$ ,  $d = 121 \mu\text{m}$  at high  $Re$  regime.

Above robust optimization deals with an optimization problem in which the set of feasible solutions are precisely provided for low and high  $Re$  regimes. However, as the factors may be uncertain, it is more practical to provide a feasible range of factors in which desirability is reasonably close to the optimal value. The desirability function for low  $Re$  exhibits a broad peak at low  $w_t$  values and low / medium  $d$  values. Therefore, it can be assumed that the uncertainty at the level of 10% in  $w_t$  and  $d$  will still result in robust solution (-1.1% change in  $D_n$ ). When considering high  $Re$  regime, the peak in desirability function is much narrower. The uncertainty at the level of 5% in  $w_t$  and  $d$  results in -3.7% change in  $D_n$ .

#### 4. Conclusions

To compare the developed micromixer with the state of the art passive planar micromixers reported in Table 1, the mixer length was evaluated, as all the reported mixers give  $M \geq 80\%$  which can be considered as a full mixing<sup>30,31</sup>. The developed mixer enables efficient fluid mixing for low ( $Re = 0.1$ ) and high  $Re$  ( $Re = 117.6$ ) using a channel much shorter (2.5 mm) than in majority of planar passive micromixer; only Shih *et al.*<sup>17</sup> have reported a mixer of comparable length (see Table 1). The combination of rhombic channel geometry, diamond-shaped obstacles and rectangular contraction placed after each rhombus has enabled to significantly reduce the mixing length:  $\sim 4 \times$  lower than the rectangular mixer with diamond-shaped obstacles (mixing length: 11.0 mm)<sup>10</sup> and  $\sim 3 \times$  lower than the rhombic (angle  $60^\circ$ ) with a converging–diverging element placed after three-rhombi channel (mixing length: 6.8 mm)<sup>14</sup>.

To find a compromise, a mixer design should be optimized to obtain high mixing efficiency with pressure drop as low as possible. As such, in this work the statistical analysis was used to determine mixer configuration that gives the best compromise between those responses. The resulting optimum geometry is  $w_t = 101 \mu\text{m}$ ,  $d = 93 \mu\text{m}$  at low  $Re$  regime and  $w_t = 400 \mu\text{m}$ ,  $d = 121 \mu\text{m}$  at high  $Re$  regime. For low  $Re$  flows, the pressure drop is low enough (6.0 Pa) for the application in lab-on-chip devices, while for high  $Re$  the mixer imposed relatively large pressure drop ( $5.1 \times 10^4$  Pa). Although, the PDMS chips sealed to glass by oxygen plasma treatment can handle pressures up to  $3.4 \times 10^5$  Pa<sup>33</sup>, i.e.  $\sim 7$  times higher than the developed mixer requires at  $Re = 117.6$ , a lower pressure drop would be beneficial for the overall device performance and for integration of the mixer with other microfluidic components. Therefore, the developed device enables efficient mixing with low pressure drop within a very short channel at low  $Re$ , making it suitable for applications where several tasks of complex analysis are needed.

Besides, results presented in this paper show that the use of statistical methods can improve significantly the data analysis enabling determination of the most important factors influencing the mixing efficiencies and pressure drop, building a mathematical model for all responses under consideration and identification of the most desirable conditions for mixer performance. Providing details of the statistical analysis (see also Supplementary Information), we aim to make this efficient mathematical strategy more available to a broader community.

In many microfluidics applications (e.g. inkjet printing; biological analysis), aqueous fluids containing low concentrations of high molecular weight polymers are used<sup>29</sup>. Therefore in future work, effect of viscoelasticity on the mixer performance will be studied.

### Acknowledgements

This work was supported by the Institute of Nanostructures, Nanomodelling and Nanofabrication, UNINOVA and by FCT-MCTES through CENIMAT/I3N (PEst-C/CTM/LA0025/2013-14) and CIGMH (PEst-OE/SAU/UI0009/2011-14) as well as by the projects EXCL/CTM-NAN/0201/2012, “SMART-EC” FP7-ICT-2009.3.9/258203, PTDC/BBB-IMG/1225/2012, Matepro – Optimizing Materials and Processes (Programa Operacional Regional do Norte (ON.2) NORTE-07-0124-FEDER-000037) and ERC Advanced Grant (INVISIBLE contract number 228144). The authors acknowledge A. C. Vaz for assistance in chip fabrication/characterization and Keep Calm and Publish Papers [keepcalmandpublishpapers.com](http://keepcalmandpublishpapers.com) video blog for graphical guidelines.

### References

1. G. M. Whitesides, *Nature*, 2006, **442**, 368-373.
2. L. Capretto, W. Cheng, M. Hill, X. Zhang and B. Lin, Springer Berlin / Heidelberg, 2011, pp. 27-68.
3. C.-Y. Lee, C.-L. Chang, Y.-N. Wang and L.-M. Fu, *Int. J. Mol. Sci.*, 2011, **12**, 3263-3287.
4. H. Wang, P. Iovenitti, E. Harvey and S. Masood, *Smart Mater. Struct.*, 2002, **11**, 662.
5. J. S. Kuo and D. T. Chiu, *Annual Review of Analytical Chemistry*, 2011, **4**, 275-296.
6. T. Burghlea, E. Segre, I. Bar-Joseph, A. Groisman and V. Steinberg, *Physical Review E*, 2004, **69**, 066305.
7. M. Kashid, A. Renken and L. Kiwi-Minsker, *Chemical Engineering Journal*, 2011, **167**, 436-443.
8. K. Conlisk and G. O'Connor, *Microfluid. Nanofluid.*, 2012, **12**, 941-951.
9. C. Chung and T. Shih, *Microfluid. Nanofluid.*, 2008, **4**, 419-425.
10. A. A. S. Bhagat, E. T. K. Peterson and I. Papautsky, *J. Micromech. Microeng.*, 2007, **17**, 1017.
11. M. A. Ansari, K.-Y. Kim, K. Anwar and S. M. Kim, *J. Micromech. Microeng.*, 2010, **20**, 055007.
12. C. K. Chung, C. Y. Wu and T. R. Shih, *Microsyst. Technol.*, 2008, **14**, 1317-1323.
13. P. Li, J. Cogswell and M. Faghri, *Sensors and Actuators B*, 2012, **174**, 126-132.
14. C. K. Chung, T. R. Shih, T. C. Chen and B. H. Wu, *Biomed. Microdevices*, 2008, **10**, 739-748.

15. C. K. Chung and T. R. Shih, *J. Micromech. Microeng.*, 2007, **17**, 2495.
16. R.-T. Tsai and C.-Y. Wu, *Biomicrofluidics*, 2011, **5**, 014103-014113.
17. T. R. Shih and C. K. Chung, *Microfluid. Nanofluid.*, 2008, **5**, 175-183.
18. R. Goovaerts, W. Smits, G. Desmet, J. Denayer and W. De Malsche, *Chemical Engineering Journal*, 2012, **211**, 260-269.
19. C. K. Chang, T. R. Shih and C. K. Chung, in *Nano/Micro Engineered and Molecular Systems (NEMS), 2011 IEEE International Conference on*, 2011, pp. 245-248.
20. T. Matsunaga, H.-J. Lee and K. Nishino, *Lab Chip*, 2013, **13**, 1515-1521.
21. L. A. Utracki, *Polymer Blend Handbook*, 2002.
22. A. D. Stroock, S. K. W. Dertinger, A. Ajdari, I. Mezic, H. A. Stone and G. M. Whitesides, *Science*, 2002, **295**, 647-651.
23. L. Hilliou, D. van Dusschoten, M. Wilhelm, H. Burhin and E. R. Rodger, *Rubber Chemistry and Technology*, 2004, **77**, 192-200.
24. D. Lee and S. H. Lee, *Journal of the Korean Physical Society*, 2008, **52**, 580-587.
25. A. A. S. Bhagat and I. Papautsky, *J. Micromech. Microeng.*, 2008, **18**, 085005.
26. I. Bernacka-Wojcik, P. Lopes, A. Catarina Vaz, B. Veigas, P. Jerzy Wojcik, P. Simoes, D. Barata, E. Fortunato, P. Viana Baptista, H. Aguas and R. Martins, *Biosens Bioelectron*, 2013, **48**, 87-93.
27. S. Lee and S. Lee, *Microsyst. Technol.*, 2008, **14**, 205-208.
28. N. J. Balmforth, A. Provenzale, N. J. Balmforth and R. V. Craster, in *Geomorphological Fluid Mechanics*, Springer Berlin Heidelberg, 2001, pp. 34-51.
29. L. E. Rodd, T. P. Scott, D. V. Boger, J. J. Cooper-White and G. H. McKinley, *Journal of Non-Newtonian Fluid Mechanics*, 2005, **129**, 1.
30. H. SadAbadi, M. Packirisamy and R. Wuthrich, *RSC Advances*, 2013, **3**, 7296-7305.
31. N. Tran-Minh, T. Dong and F. Karlsen, *Computer Methods and Programs in Biomedicine*, 2013, **117**, 20-29.
32. G. Derringer and R. Suich, *Journal of quality technology*, 1980, **12**, 214-219.
33. J. C. McDonald, D. C. Duffy, J. R. Anderson, D. T. Chiu, H. K. Wu, O. J. A. Schueller and G. M. Whitesides, *Electrophoresis*, 2000, **21**, 27-40.

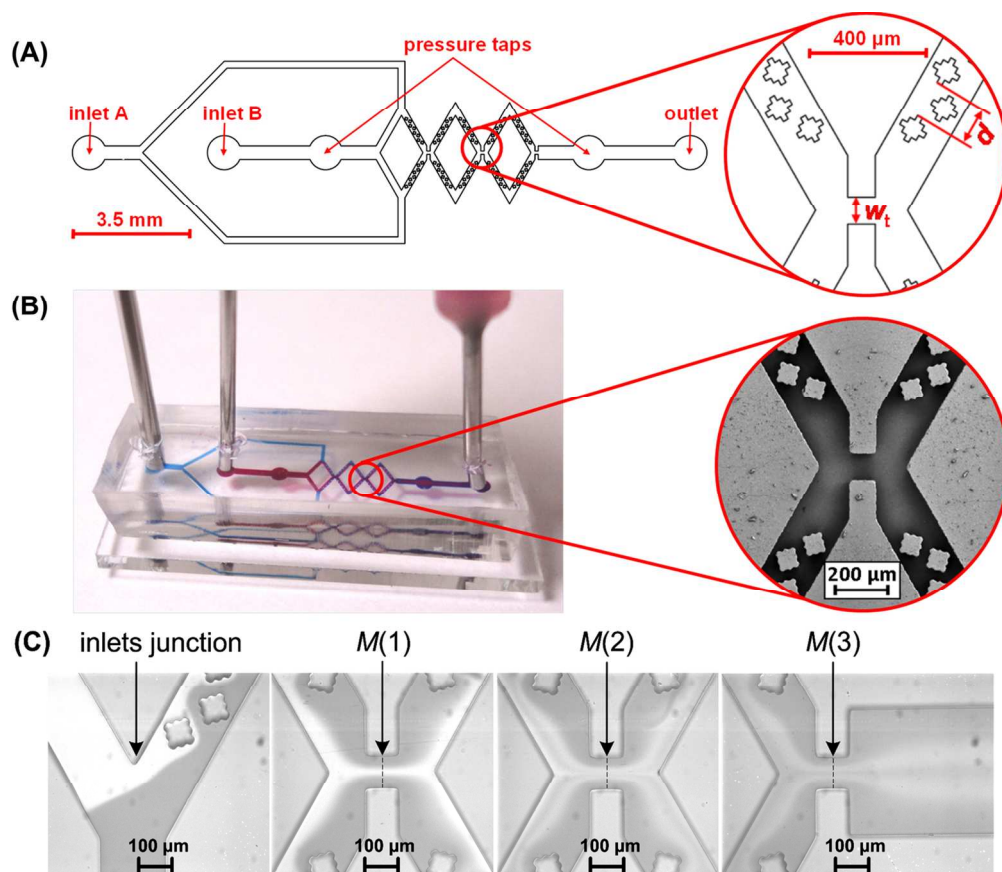


Fig. 1. (A) Schematic diagram of the designed rhombic micromixer with stepped diamond-shaped obstacles and rectangular contractions between rhombi. (B) PDMS micromixer fabricated using SU-8 mould and epoxy mediating mould. (C) Optical microscopy images taken at different locations along a micromixer with  $w_t = 100\ \mu\text{m}$  and  $d = 140\ \mu\text{m}$  at  $Re = 8.2$ . Mixing efficiency was analysed along the channel in the middle of the first contraction, M(1), second contraction, M(2) and third contraction, M(3), as indicated by the vertical dotted lines.

135x117mm (300 x 300 DPI)

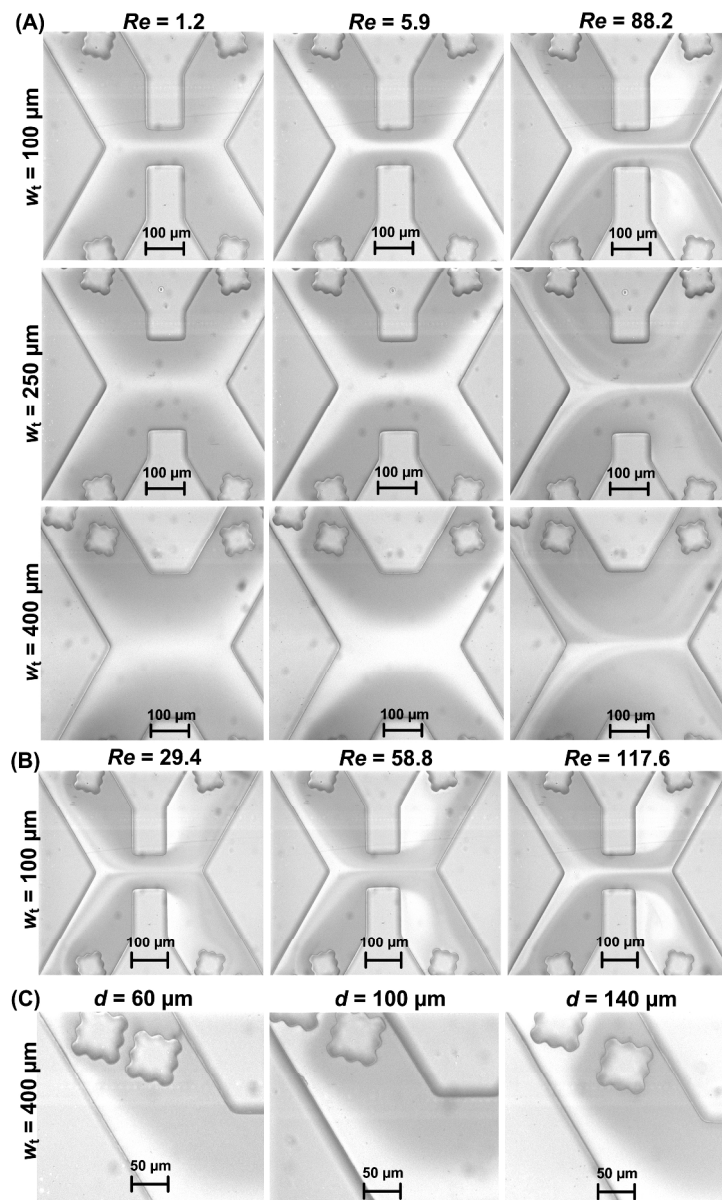


Fig. 2. Optical microscopy images taken at the first contraction for various flow conditions. (A) Influence of the contraction width ( $w_t$ ) on fluid mixing at  $Re = 1.2$ ;  $Re = 5.9$  and  $Re = 88.2$ , in mixers with inter-obstacles distance  $d = 140 \mu\text{m}$ . At lower  $w_t$  and higher  $Re$ , strong acceleration and subsequent deceleration of flows leads to formation of vortices. (B) Comparison of vortices generated at  $Re = 28.4$ ;  $Re = 58.8$  and  $Re = 117.6$  in mixer with  $w_t = 100 \mu\text{m}$ . (C) Influence of the inter-obstacles distance ( $d$  varying from  $60 \mu\text{m}$  to  $140 \mu\text{m}$ ) for micromixers with  $w_t = 400 \mu\text{m}$  at  $Re = 5.9$ . For  $d = 60 \mu\text{m}$ , the fluids flow mainly next to the channel walls due to low inter-obstacles channel width.

235x390mm (300 x 300 DPI)

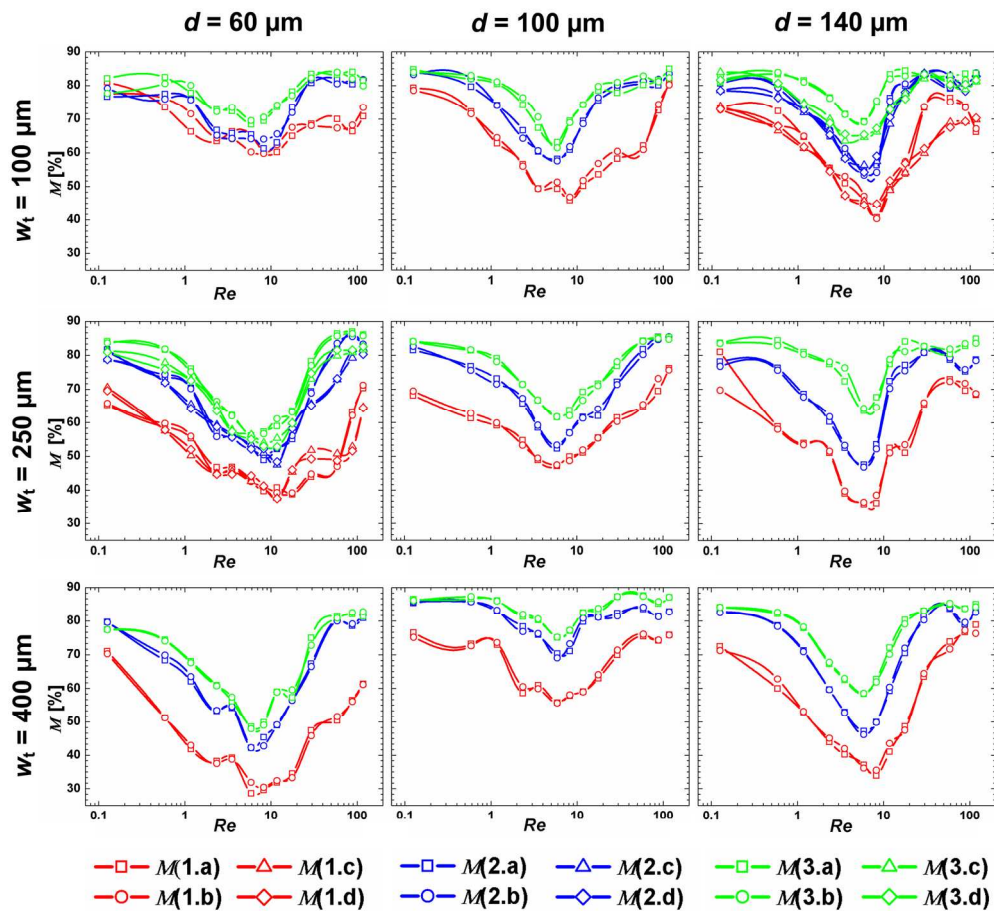


Fig. 3. Experimental mixing efficiency ( $M$ ; given in %) of mixers with various configurations at the middle of the first contraction ( $M(1)$ ; red line), second contraction ( $M(2)$ ; blue line) and third contraction ( $M(3)$ ; green line). Data points labelled a and b were determined from two different images taken from the first chip, while data points labelled c and d were determined from two different images taken from the second chip.

Connecting lines are for eye guidance only.

173x158mm (300 x 300 DPI)

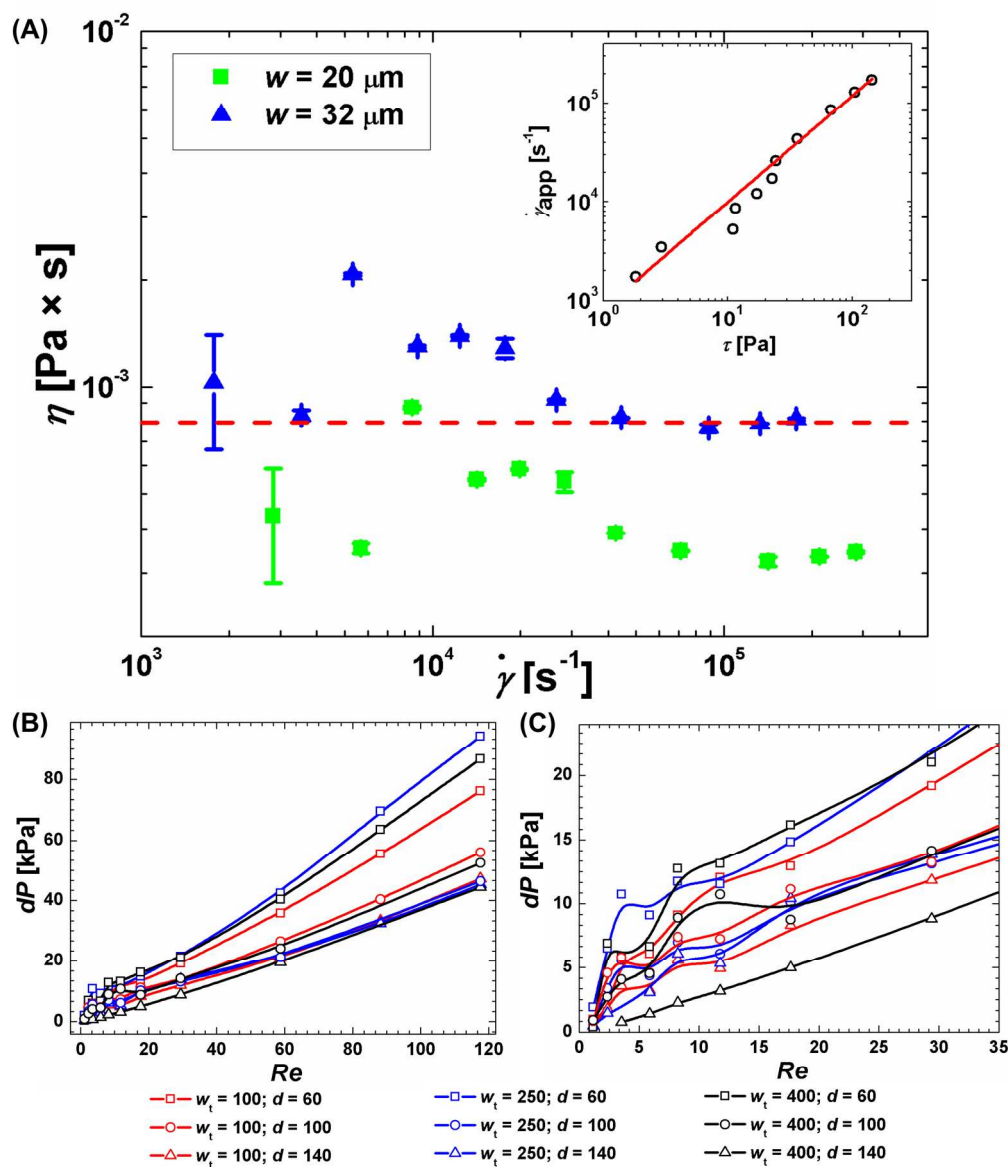


Fig. 4. (A) Shear rate dependence of the shear viscosity computed from the pressure drop ( $dP$ ) and the volumetric flow rate ( $Q$ ) measured with chip of  $w_t = 100 \mu\text{m}$ ;  $d = 60 \mu\text{m}$  for two values of the effective channel width ( $w$ ):  $20 \mu\text{m}$  (squares) and  $32 \mu\text{m}$  (triangles). The red dashed horizontal line indicates the viscosity ( $8 \times 10^{-3}$  Pa  $\times$  s) of water at 28 °C measured with a rotational rheometer. Inset: stress dependence of the apparent shear rate. The red line is a linear fit to the data with slope of  $1.08 \pm 0.07$  indicating a Newtonian behavior. (B) Experimental pressure drop ( $dP$ ) for micromixers of various configurations ( $w_t$  and  $d$  are given in  $\mu\text{m}$ ). (C) Zoom in on the low  $Re$  region. For low  $dP$  values (usually below 12), there is no linear dependence between  $dP$  and  $Re$  due to the detection limit of the pressure sensor.

186x218mm (300 x 300 DPI)

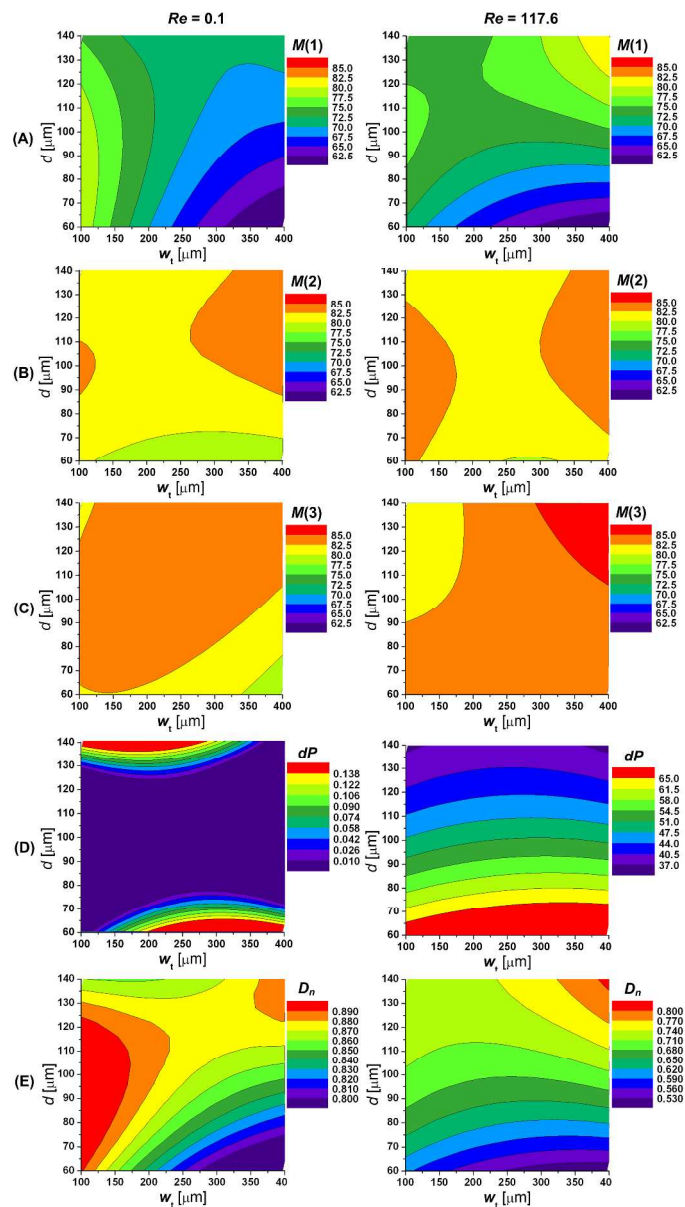


Fig. 5. Results obtained from mathematical fitting to the experimental data points (A) of mixing efficiency (given in %) measured at the middle of the first contraction (M(1)); (B) at the second contraction (M(2)); (C) at the third contraction (M(3)) and (D) of pressure drop (dP; given in kPa) measured after three rhombi. (E) Desirability results ( $D_n$ ) defined as maximum values of M(1); M(2) and M(3) and minimum of dP.  
279x489mm (300 x 300 DPI)

A short passive planar micromixer was experimentally optimised using statistical methods to determine parameters significance and most desirable geometry.

